Electronic supplementary materials
For https://doi.org/10.1631/jzus.A2500194

Effect of laminar plasma quenching technology on the anti-wear and anti-fatigue properties of two types of U75V rail welded joints

Jingmang XU[1,2], Hui ZHU[1,2], Wenfeng GAO[1,2], Taoshuo BAI[1,2], Jian YANG[1,2], Kai WANG[3], Yao QIAN[1,2], Ping WANG[1,2]

[1] *MOE Key Laboratory of High-speed Railway Engineering, Southwest Jiaotong University, Chengdu 610031, China*
[2] *School of Civil Engineering, Southwest Jiaotong University, Chengdu 610031, China*
[3] *College of Design and Engineering, National University of Singapore, Singapore 117356, Singapore*

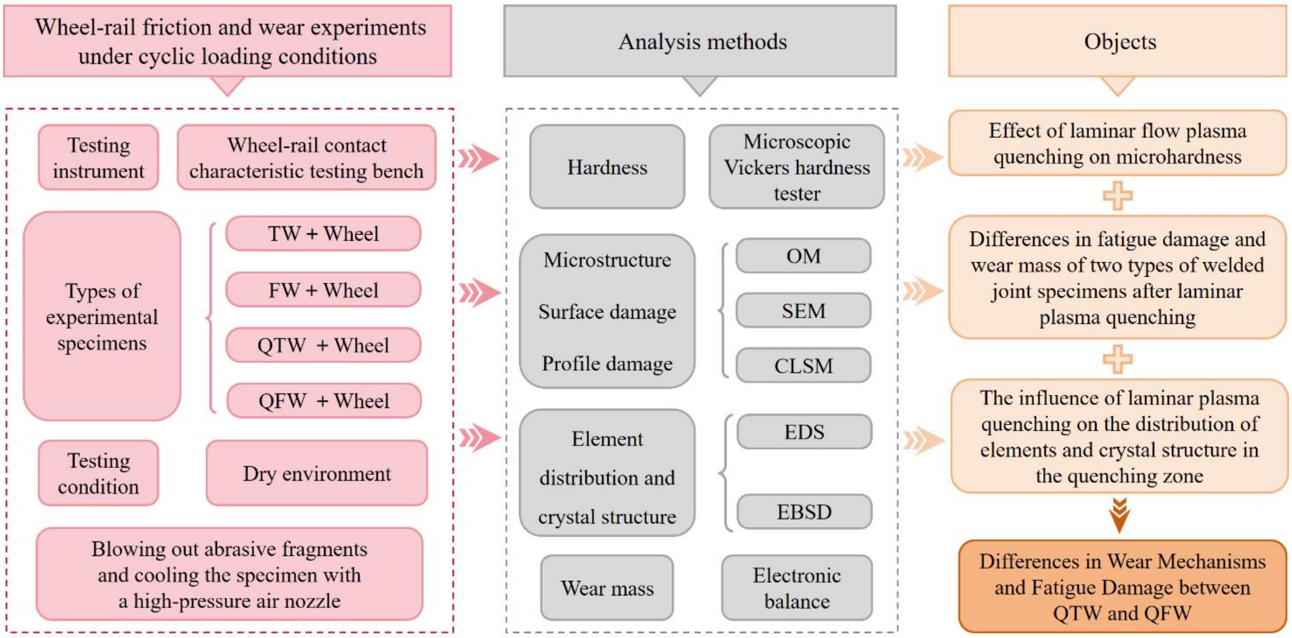

Fig. S1 Flowchart of this experiment.

S1 Analysis of rail welded joints in the field

U75V rails with thermite welded joints and flash-butt welded joints and CL60 wheels were used as experimental materials. The chemical composition and mechanical properties of the rails and wheels are presented in Tables S1 and S2, respectively (Hu et al., 2020; Hu et al., 2021).

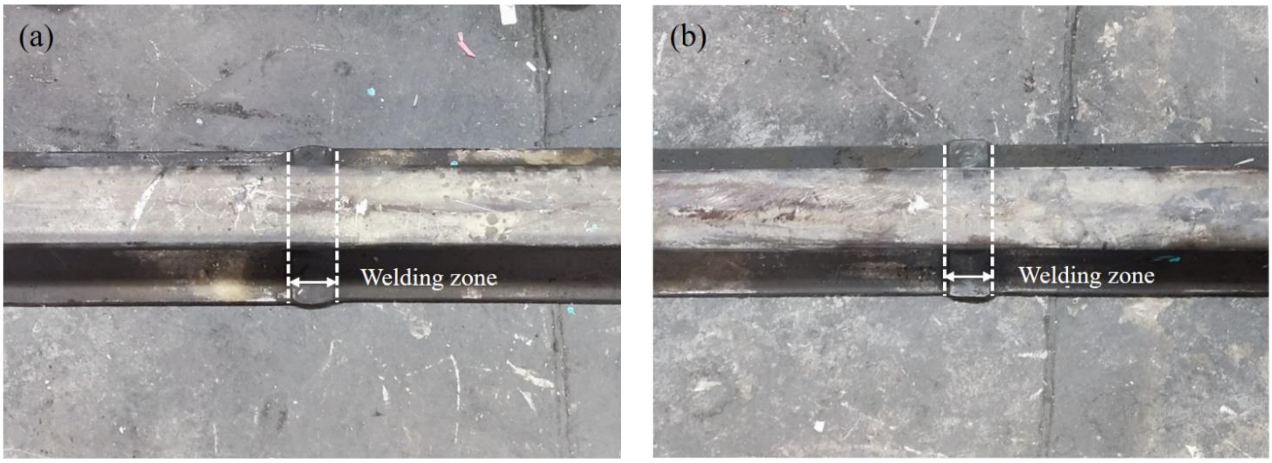

Fig. S2 Field photographs of welding joints in rails: (a) TWJ; (b) FWJ.

Table S1 Chemical composition of specimens (wt%) (Hu et al., 2020; Hu et al., 2021).

Material	Chemical composition					
	C	Si	Mn	P	S	V
Wheel (CL60)	0.55–0.65	0.17–0.37	0.50–0.80	0.025	0.025	0.06
Rail (U75V)	0.71–0.80	0.50–0.80	0.70–1.05	≤0.025	≤0.025	0.04–0.12

Table S2 Mechanical properties of specimens.

Material	σ_b (MPa)	σ_s (MPa)	δ (%)	ψ (%)	$HV_{0.5}$
Wheel (CL60)	≥910	≥580	≥12	≥14	290–360
Rail (U75V)	≥980	≥610	≥10	≥14	280–320

In this experiment, U75V rail substrates were welded together using both thermite welding and flash-butt welding processes. The flash-butt welding process heats the ends of the rails to a surface melting state by applying an electric current, followed by the application of a forging force. Under pressure, the metals at both rail ends crystallize together, effectively welding the two steel rails. The thermite welding process requires preheating the welding area before igniting the aluminum thermal agent, which undergoes a vigorous oxidation-reduction reaction that generates high-temperature molten metal. This molten metal is then directionally cast into a sand mold to weld the two rails together. The specific welding processes and parameters for the two types of welded joints are illustrated in Fig. S3. According to previous studies on the impact wear of these two types of welded joints, there are certain differences in the microstructure of their various zones, resulting in significant variations in their mechanical properties (Li et al., 2021). This section will provide a detailed analysis of these two types of joints and will serve as the foundation for subsequent experiments.

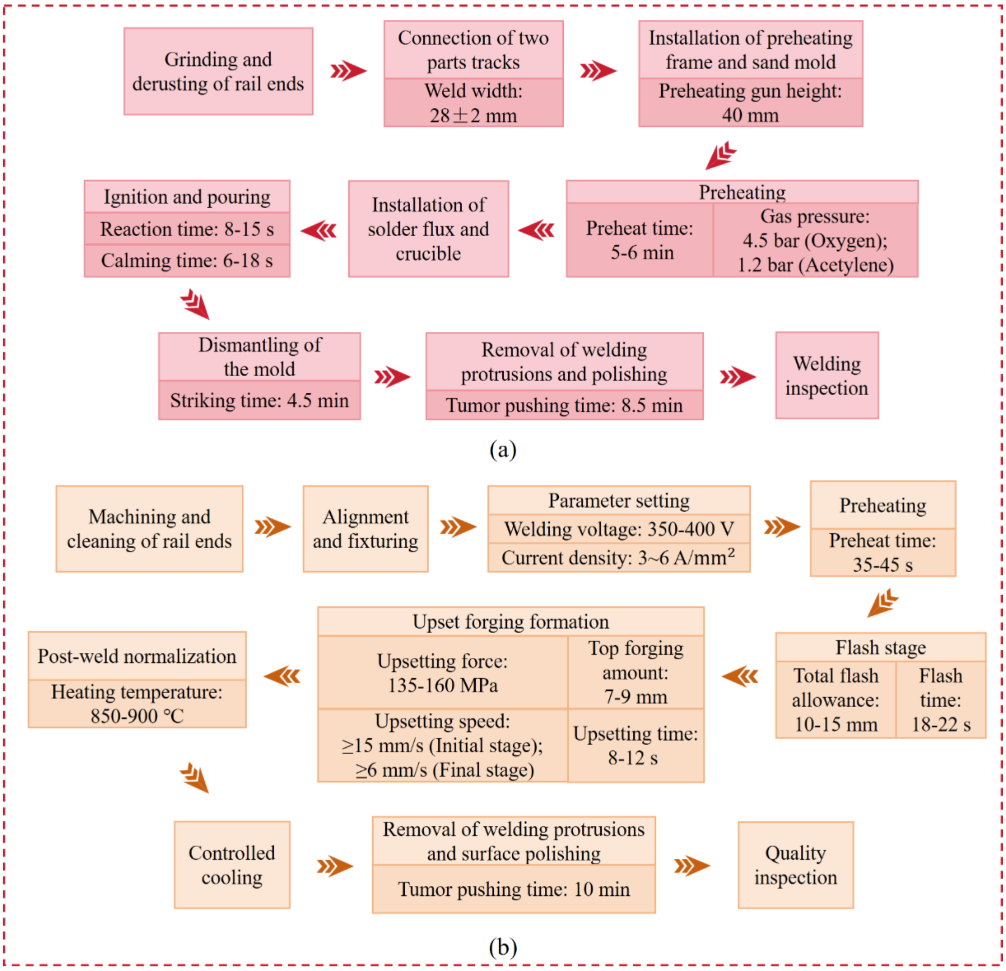

Fig. S3 Flow chart of welding process for rail welded joint: (a) TWJ; (b) FWJ.

S1.1 Hardness

Due to the different welding processes, the two types of welded joints exhibit distinct hardness distributions. The hardness of the weld bead (WB) zone, heat affected (HA) zone, and base material (BM) zone of thermite/flash-butt welded joints was measured every 2 mm along the longitudinal direction of the rail using a Vickers hardness tester (HVS-1000Z, Suzhou). Given the heterogeneity of the welded joints, each position was measured three times, and the average value was recorded. The trend in hardness change is illustrated in Figs. S4(a) and S4(b). It can be observed that the width of the WB zone for both types of welded joints is approximately 80-90 mm. After measurement, the average hardness of the two types of joint substrates was found to be about 313.1 $\mathrm{HV}_{0.5}$. Furthermore, the average hardness of the WB zone and HA zone in TWJ is lower than that of the corresponding zones in FWJ, with a more significant decrease in hardness observed in TWJ.

A cross-section was cut in various zones of the two welded joints, and the hardness was measured every 0.4 mm along the depth direction of each cross-section. The average hardness values for the cross-sections are presented in Figs. S4(c) and S4(d). In the depth direction, from the near surface to the interior, the hardness of both types of joints exhibits a decreasing trend, indicating a certain commonality. Specifically, in TWJ, the hardness of the WB and BM zones is significantly higher than that of the HA zone. At the near surface position of the rail, the hardness values for the WB and BM zones are relatively close, with Vickers hardness values ranging from 370 to 400 $\mathrm{HV}_{0.5}$, while the hardness of the HA zone is considerably lower, at approximately 340 $\mathrm{HV}_{0.5}$. In the near surface region of FWJ, the hardness range for the WB and BM zones is between 370 and 400 $\mathrm{HV}_{0.5}$; however, the hardness of the HA zone is higher than that of the TWJ at the same position, measuring 360 $HV_{0.5}$. An analysis of the intrinsic mechanisms underlying the changes in hardness reveals that both joints are influenced by the work hardening effect generated by the rolling-sliding contact between the wheel and the rail. As the depth increases, this work hardening effect gradually diminishes, leading to a stabilization of hardness after a significant decrease.

In addition, to obtain the variability in the three hardness measurements, we calculated the standard deviation of the measured hardness values. The average standard deviations for the WB, HA, and BM zones in the FWJ are 2.85 $HV_{0.5}$, 7.82 $HV_{0.5}$, and 1.94 $HV_{0.5}$, respectively, while those for the WB, HA, and BM zones in the TWJ are 6.26 $HV_{0.5}$, 11.32 $HV_{0.5}$, and 2.14 $HV_{0.5}$, respectively. These standard deviation values clearly reflect the complexity and heterogeneity of the microstructure across the various zones of the welded joints.

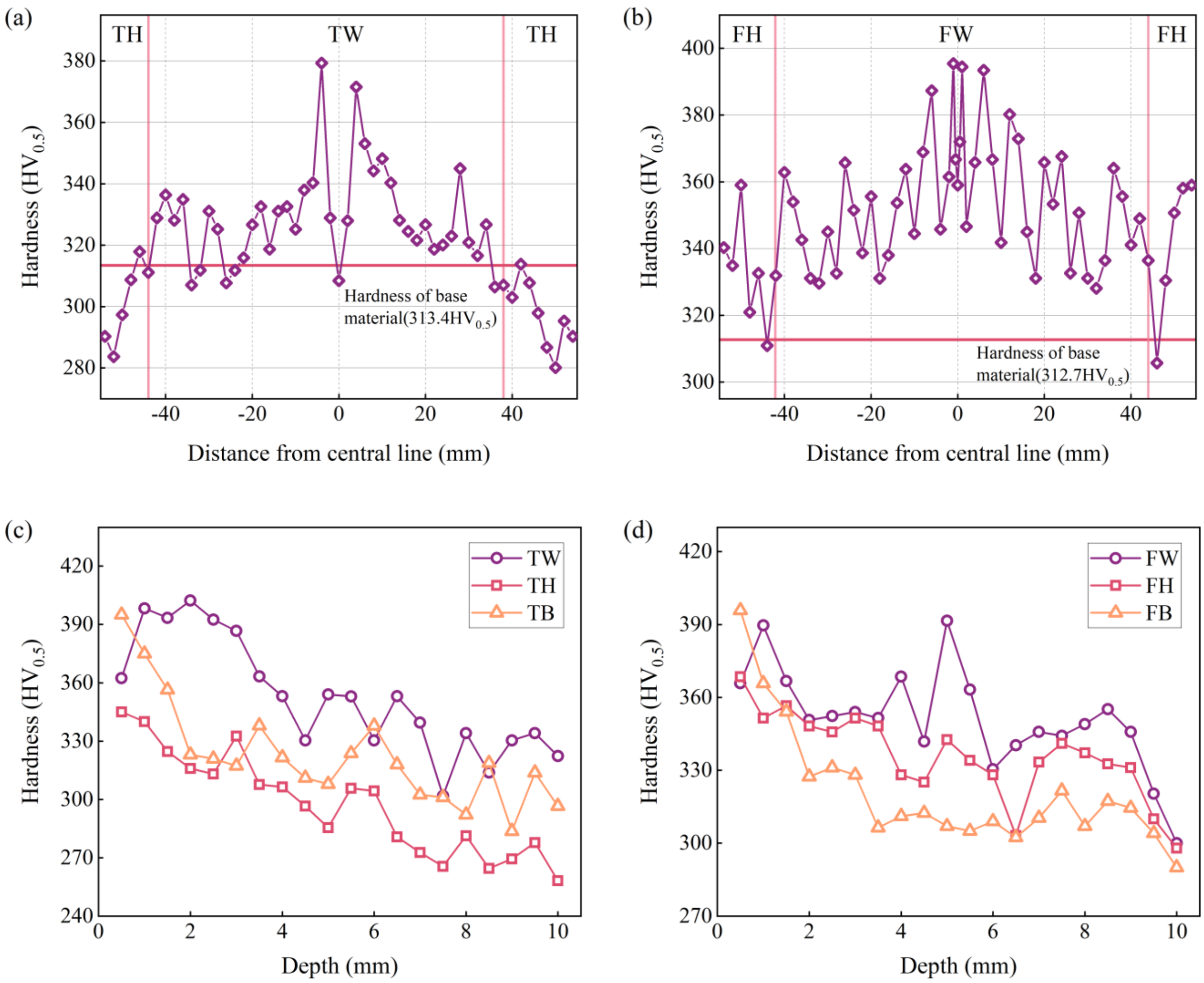

Fig. S4 Hardness distribution of standard rail welding joints: (a) Hardness of TWJ in the longitudinal direction; (b) Hardness of FWJ in the longitudinal direction; (c) Hardness of TWJ in cross-section; (d) Hardness of FWJ in cross-section.

S1.2 Microstructure

Figs. S5(a) and S5(b), as well as Figs. S6(a) and S6(b), illustrate the microstructural composition of the weld bead zone in thermite welded joints (TWB) and flash-butt welded joints (FWB). The microstructure of TWB is composed of pearlite with large interlayer spacing, while the microstructure of FWB consists of both pearlite and ferrite, with ferrite present in the gaps between the grains. From a formation mechanism perspective, the microstructure of TWB is formed due to the significant growth of austenite grains, which is induced by the high temperatures generated from the aluminum thermal reaction, along with the development of a coarse pearlite structure at a lower air-cooling rate. In contrast, the microstructure of FWB is caused by the instantaneous temperature surge at the contact surface due to resistance heating, which leads to the damage of carbon elements and the precipitation of a network-like ferrite structure after cooling. Furthermore, the possible presence of martensite in TWB may contribute to an uneven overall structure, thereby reducing joint toughness and increasing the risk of brittle fracture (Li et al., 2021). The network ferrite in FWB can also adversely affect the overall mechanical properties of the joint. Figs. S5(c) and S5(d), as well as Figs. S6(c) and S6(d), illustrate the microstructural characteristics of the heat-affected zone in both the thermite welded joints (THA) and flash-butt welded joints (FHA). The THA exhibits a spherical pearlite structure characterized by noticeable graininess and irregular grain sizes, while the FHA displays a mixed structure comprising a small amount of ferrite and granular pearlite, resulting in a loose organization. The formation mechanisms of THA and FHA are similar. The microstructure of THA is caused by uneven thermal distribution, leading to changes in carbides, while the microstructure of FHA results from incomplete crystallization and insufficient dissolution of carbides due to uneven heating (Li, et al., 2021). Additionally, fluctuations in the composition of the thermite during the thermite welding process can also affect the uniformity of the microstructure within the heat-affected zone. The disordered distribution of microstructure in this zone contributes to its inferior mechanical properties compared to the rest of the joint. Observations under OM and SEM reveal that the base material of both TWJ and FWJ possesses a uniform pearlite structure, as depicted in Figs. S5(e) and S5(f) and Figs. S6(e) and S6(f). The pearlite is arranged linearly, exhibits uniform density, and has small interlayer spacing, which results in stable mechanical properties, high hardness, and excellent fatigue resistance in the base material.

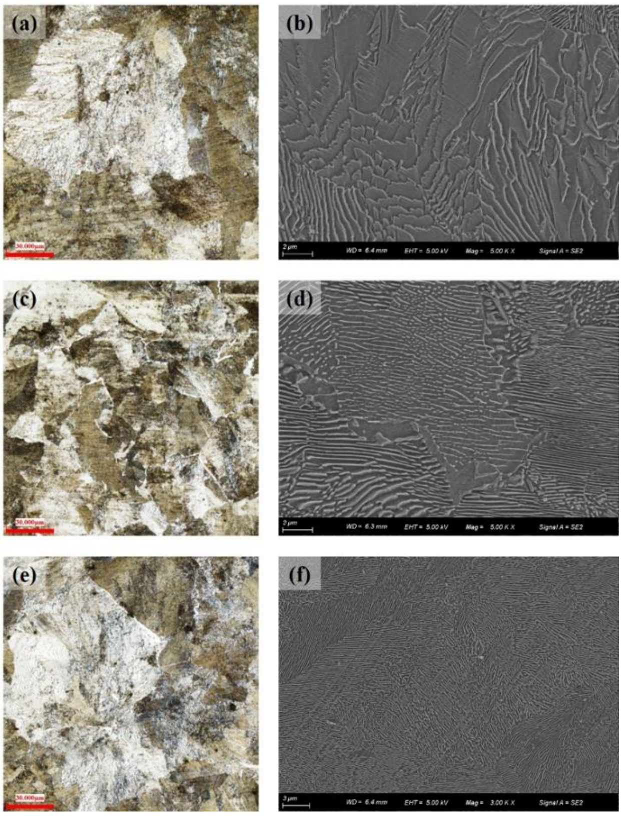

Fig. S5 OM and SEM images of the microstructure of the TWJ: (a, b) WB; (c, d) HA; (e, f) BM

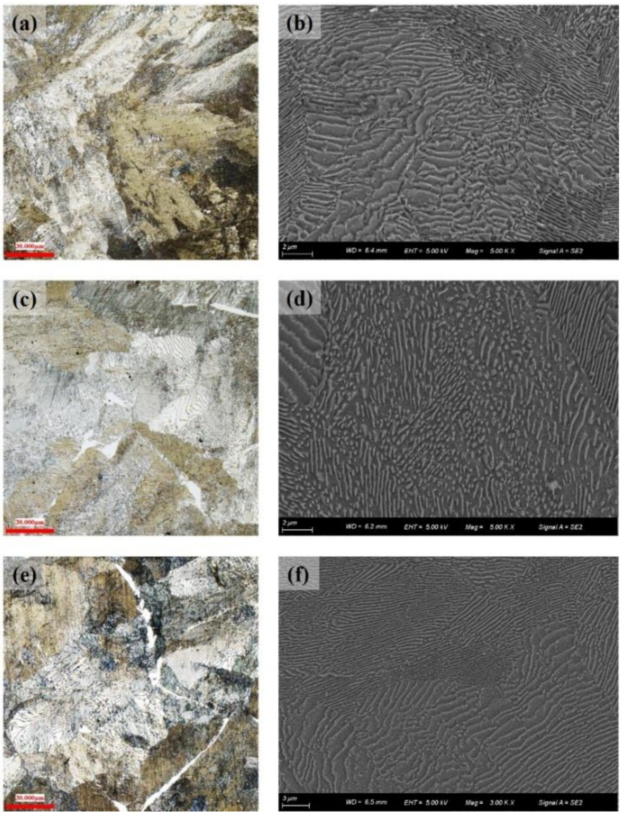

Fig. S6 OM and SEM images of the microstructure of the FWJ: (a, b) WB; (c, d) HA; (e, f) BM

S1.3 Fatigue damage

Fig. S7 shows the surface morphology and profile damage of standard rail welded joints. A long surface crack was observed on the surface of the flash-butt welded joint, which was confirmed to extend downward to a depth of 4,800 μm through profile measurements. Notably, the crack branched out during its propagation. Additionally, a spalling pit approximately 60 μm deep was identified in the specimen profile, as depicted in Fig. S7(a). In the case of thermite welded joints, damage primarily manifested as fine cracks on the specimen's surface, accompanied by a high density of spalling pits, as shown in Figs. S7(c) and S7(d). It can be hypothesized that the continuous propagation of surface microcracks leads to the removal of the material above them, resulting in the formation of spalling pits, which exemplifies the typical phenomenon of wear removal fatigue cracking.

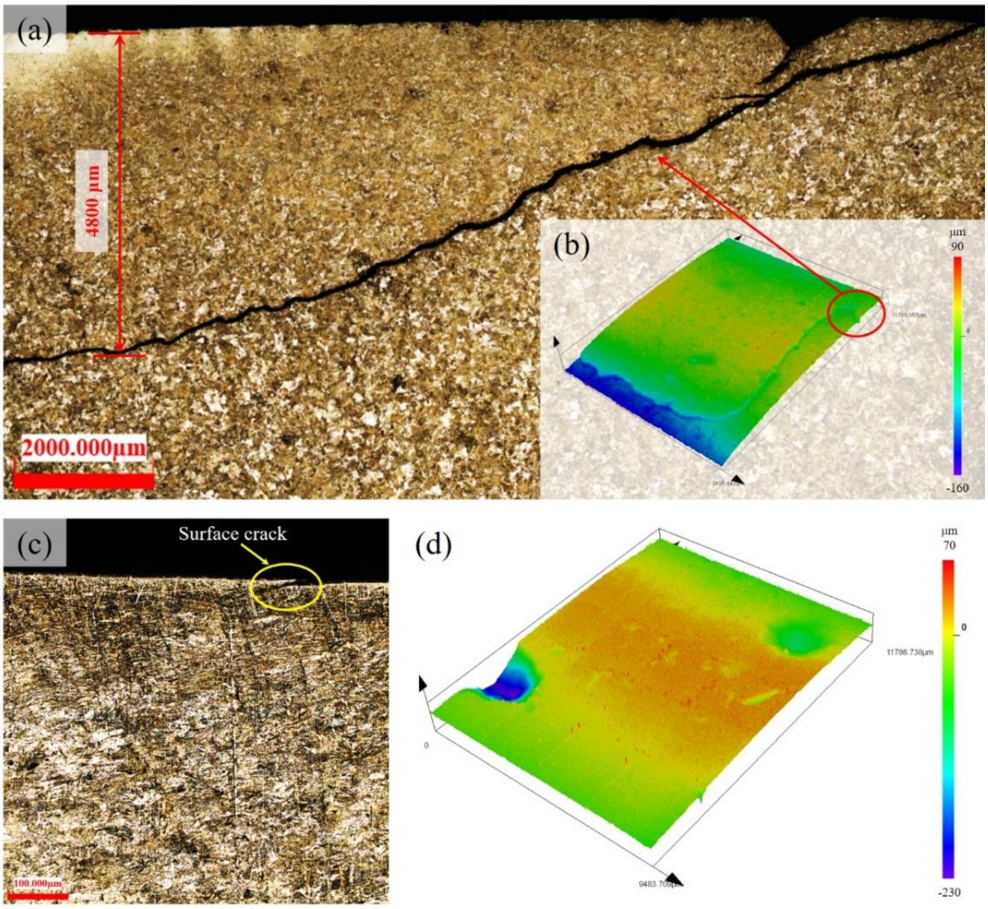

Fig. S7 Surface and sectional damage of standard rail welded joints: (a, b) FWJ; (c, d) TWJ.

Table S3 Characterization and analysis methods after the experiment.

Testing instruments and methods	Testing object
JA4103 electronic balance	Wear mass of specimen
Micro-hardness tester (HVS-1000Z)	Hardness of the cross-section of the specimens
Field emission scanning electron microscope (SIGMA-500); Confocal laser scanning microscope (LSM-900)	Microscopic morphology of the surface of the specimens
Field emission scanning electron microscope (SIGMA-500); Optical microscope (GT-K)	Microstructure of the cross-section of the specimens
Energy Dispersive Spectrometer	Chemical composition of the cross-section of the specimens
Electron Back Scatter Diffraction	Crystallographic properties of material in the quenching zones

References

Hu Y, Zhou L, Ding HH, et al., 2020. Investigation on wear and rolling contact fatigue of wheel-rail materials under various wheel/rail hardness ratio and creepage conditions. *Tribology International*, 143:106091. https://doi.org/10.1016/j.triboint.2019.106091

Hu Y, Watson M, Maiorino M, et al., 2021. Experimental study on wear properties of wheel and rail materials with different hardness values. *Wear*, 477:203831. https://doi.org/10.1016/j.wear.2021.203831